Magnetic-field-induced spin texture in a quantum wire with linear Dresselhaus spin-orbit coupling

S. Gujarathi, K. M. Alam, and S. Pramanik*

Department of Electrical and Computer Engineering, University of Alberta, Edmonton, AB T6G 2V4, Canada

(Received 3 September 2011; revised manuscript received 11 December 2011; published 6 January 2012)

A quantum wire with strong Rashba spin-orbit interaction is known to exhibit a so-called spin texturing effect in presence of a moderate external magnetic field acting transverse to the wire axis and parallel to the symmetry-breaking "gate" electric field causing Rashba interaction. This effect typically disappears when the external magnetic field is made stronger than the effective spin-orbit magnetic field due to the Rashba interaction. In this work, we present a detailed study of the spin texturing phenomenon in a quantum wire with strong linear Dresselhaus spin-orbit interaction and an external transverse magnetic field. Unlike the pure Rashba case, we observe a persistent spin texture even in the limit when the external magnetic field is large and much stronger than the effective spin-orbit magnetic field due to Dresselhaus interaction. Magnetic field dependence of spin texture is therefore an experimentally viable method for identifying the dominant spin-orbit interaction in a zinc-blende quantum wire. We show that the local distribution of the spin density can be modulated by spin-orbit coupling strength, magnetic field, and the Fermi level of the electron gas.

DOI: 10.1103/PhysRevB.85.045413 PACS number(s): 71.70.Ej, 85.75.−d, 75.70.Tj, 81.07.Vb

I. INTRODUCTION

Spin-orbit interaction in quantum confined structures has attracted immense interest due to its fundamental role in virtually all spintronic devices.[1] In particular, electrical control of spin-orbit interaction is the basis of many embodiments of the spin field effect transistor.[2–4] However, spin-orbit interaction is also the main ingredient of Elliott-Yafet and D'yakonov-Perel' spin relaxation, which limit spin lifetime and are detrimental to spintronic device operation.[5]

Two major spin-orbit interactions that are gate-tunable in quantum confined systems,[2–4] and hence crucial for many spintronic applications are (a) Rashba effect, which arises when an electron experiences a strong electric field due to the asymmetry in the confinement potential (or structural inversion asymmetry)[6] and (b) Dresselhaus interaction, which appears due to the microscopic electric field arising from the lack of inversion symmetry in the Bravais lattice (or bulk inversion asymmetry).[7] These spin-orbit interactions lift the spin degeneracy of the subbands for nonzero wave vectors (so-called "zero-field spin splitting," which is observed in the beating pattern of Shubnikov-de Haas oscillations),[8,9] introduce nontrivial features in the energy spectrum and form the basis of many spintronic devices as described in Refs. 3,4,10,11. Presence of an external magnetic field introduces additional complexities in the subband structure. Many single-particle, effective-mass calculations employ a so-called zeroth order model in which the spinor part of the wave function is assumed to be independent of spatial coordinates. This assumption fails to account for several intricacies of the energy spectrum as well as many spin-dependent phenomena, which have been discussed in Refs. 12–17.

In this paper, we focus on a "spin texturing effect,"[18] which typically manifests in quantum confined systems in the presence of spin-orbit interactions and external agents such as magnetic field,[15] transport driving electric field,[19,20] and terahertz radiation.[21,22] Spin texturing, also known as spin accumulation[19] or spin density modulation,[20,21] is a spatial variation of ensemble averaged spin polarizations transverse to the quantum wire channel. The concept of spin texturing is crucial for spintronics due to many reasons. First, this concept is closely related to that of spin current, since in many instances, spin current is measured as a change in the local spin density.[20] The definition of spin current is still a topic of much debate, but the above picture is experimentally accessible since it is possible to measure local spin density in a sample by various experimental techniques.[19,23–25] Spin texture is also important since it represents the spatial distribution of the effective magnetic field due to spin-orbit interaction, a knowledge of which is crucial for spintronic devices.[26]

The factors that critically influence spin texturing are external (transport driving) electric field, magnetic field, spin-orbit coupling strength, and the confinement potential.[19] However, the complex interplay of these effects is still largely unexplored. Reference 15 considered the case when the spin-orbit interaction is of Rashba type and an external transverse magnetic field is present. Reference 20 considered combined presence of Rashba and Dresselhaus interaction in a one-dimensional superlattice. In this case, spin texture can be tuned by an external electric field. The effect of terahertz radiation on similar structures has been reported in Refs. 21 and 22.

In this work, we focus on a relatively less studied scenario where spin texture is induced by an external magnetic field. We note that such situation arises frequently in experiments that measure the local spin density of the sample by techniques such as (a) spin-polarized scanning tunneling microscopy (SP-STM),[24] (b) magnetic resonance force microscopy (MRFM),[25] and most importantly, (c) optical techniques,[19,23] since all these methods employ an external magnetic field. We consider the linear Dresselhaus spin-orbit interaction, which is always present in systems with a zinc-blende structure (irrespective of any other spin-orbit interaction) and is particularly dominant in structures with strong and symmetric confinement potential. Our goal is to isolate and investigate the combined effect of Dresselhaus spin-orbit interaction and the external magnetic field on spin texturing, since these factors will always be present in spin-texture measurement experiments performed on III-V nanostructures.[19,23]

In this work, we report the subband structure and the spin texture in a III-V quantum wire with hard-wall confinement for

a wide range of magnetic field, Dresselhaus coupling strength, and carrier concentration. We find a sinusoidal variation in the spin accumulation, which is strongly dependent on the above-mentioned parameters. The spin vector is out-of-plane and the spin component along the channel axis changes sign for the two edges of the quantum wire, which is reminiscent of the spin Hall effect.[19] The spin component along the magnetic field, however, has the same sign for two edges. We offer a simple physical picture that explains these features. Quite counterintuitively, unlike the pure Rashba case,[15] we observe the spin texture to persist even when the external magnetic field is large. Thus magnetic field dependence of spin texture can be used as a viable experimental method to identify the dominant spin-orbit interaction in a zinc-blende quantum wire.

This article is organized as follows. In Sec. II, we first introduce our model describing the Dresselhaus spin-orbit interaction in a quantum wire and then outline the numerical method used to solve the nonrelativistic Pauli equation in this system. This will be followed by results and discussion in Sec. III, which describes the magnetoelectric subbands and demonstrates the magnetic field induced spin texturing effect in presence of Dresselhaus spin-orbit interaction. We conclude in Sec. IV.

II. MODEL AND METHODS

In this work, we adopt a coordinate system in which $\hat{x}$, $\hat{y}$, and $\hat{z}$ are oriented along cubic crystallographic axes [100], [010], and [001], respectively. These directions are defined in a III-V primitive cell in which the anion (such as As) resides at (0,0,0) and the cation (e.g., Ga, In, etc.) is located at $(\frac{1}{4},\frac{1}{4},\frac{1}{4})$. This specification uniquely determines the sign of the Dresselhaus constant α.[27,28] We note that in some works (for example, Ref. 29) the cation is placed at the origin, which makes the Dresselhaus constant negative.

We consider a two-dimensional electron gas (2DEG) grown along $\hat{y}$. The corresponding confinement potential $V_y(y)$ is determined by the layer sequence of the semiconductor heterostructure. There also exists a transverse confinement potential $V_z(z)$ and the quantum wire is infinitely long along $\hat{x}$. Unlike many previous reports that considered parabolic confinement (e.g., Refs. 12,13,30–34), in this work, we assume both confinement potentials to be "hard-wall," i.e.,

$$V_y(y) = 0 \text{ for } 0 \leqslant y \leqslant W_y \text{ and } \infty \text{ otherwise},$$
$$V_z(z) = 0 \text{ for } 0 \leqslant z \leqslant W_z \text{ and } \infty \text{ otherwise}.$$

Quantum wires with hard-wall confinement can be realized by various methods such as implantation-enhanced interdiffusion technique,[35,36] molecular beam epitaxy double growth technique (or cleaved-edge overgrowth)[37] and overgrowth on patterned surfaces using molecular beam epitaxy.[38] A schematic of this system is shown in Fig. 1.

We choose the confinement along $\hat{y}$ to be much stronger ($W_y << W_z$) such that only the lowest subband is occupied in this direction under all operating conditions. The electron motion is confined in the xz plane. For the purpose of numerical computation, the material parameters are chosen to be consistent with indium arsenide (InAs) with an effective mass $m^* = 0.03m_0$ (m_0 is the free electron mass) and Landé g factor = −15. This material is a narrow-gap semiconductor with strong Rashba constant that can result in significant spin-orbit coupling in presence of a confining potential with structural inversion asymmetry (SIA). However, due to the symmetric confinement potentials as shown in Fig. 1, this interaction is absent. The major source of spin-orbit interaction in this system is the Dresselhaus term, which originates due to the bulk inversion asymmetry (BIA) of InAs, which has a zinc-blende structure and therefore lacks a center of inversion. In the absence of an external magnetic field, the Dresselhaus spin-orbit interaction is responsible for lifting the twofold spin degeneracy for nonzero wave vectors.

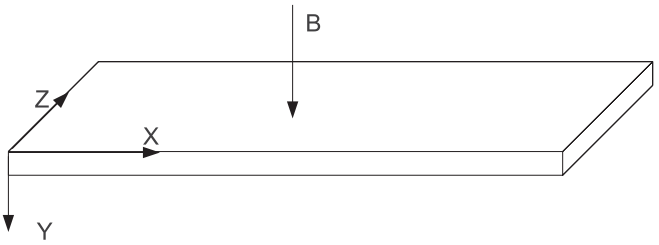

FIG. 1. Quantum wire with a rectangular cross section. The widths along $\hat{y}$ and $\hat{z}$ are given by W_y and W_z, respectively, and $W_y << W_z$ so that only one subband is occupied along $\hat{y}$ but many are occupied along $\hat{z}$. Confining potentials are hard-wall type as described in the text.

As shown in Fig. 1, a magnetic field is present along the growth direction ($\hat{y}$), which can originate, for example, from a ferromagnetic tip in spin-polarized scanning tunneling microscopy[24] or magnetic resonance force microscopy[25] experiments. In the Landau gauge $\vec{A} = (Bz,0,0)$, the single-particle effective mass Hamiltonian of this system is given by

$$H = \left[\frac{(p_x + eBz)^2}{2m^*} + \frac{p_z^2}{2m^*} + V_z(z)\right]\sigma_0 - \frac{g\mu_B \vec{B}\cdot\vec{\sigma}}{2} + H_D^{\mathrm{QW}i,B}. \quad (1)$$

In Eq. (1), the first term represents the kinetic and potential energy contributions, where $\vec{p}$ is the electron momentum and σ_0 is the 2×2 identity matrix. The second term represents the Zeeman splitting, where μ_B denotes the Bohr magneton and $\vec{\sigma}$ is the Pauli spin matrix. The term $H_D^{\mathrm{QW}i,B}$ represents the Dresselhaus Hamiltonian for the quantum wire in presence of $B\hat{y}$.

A. Dresselhaus spin-orbit interaction

In absence of any external magnetic field, the Dresselhaus term for a bulk III-V semiconductor has the following form:[39]

$$H_D^{\mathrm{bulk}} = \frac{\hbar}{2}\vec{\sigma}\cdot\vec{\Omega}(p), \quad (2a)$$
$$\Omega_x(p) = \mathcal{C}p_x\left(p_y^2 - p_z^2\right), \quad \mathcal{C} = \frac{\alpha}{\hbar m^{*3/2}\sqrt{2E_g}}, \quad (2b)$$

where E_g is the band gap, α is a numerical coefficient representing the spin-splitting of the conduction band, and the

components $\Omega_y(p),\Omega_z(p)$ are obtained from Eq. (2b) by the cyclic transposition of the indices: $x \to y \to z \to x$.

For the quantum wire described above, the Dresselhaus Hamiltonian can be obtained by replacing $\vec{\Omega}(p)$ by its average value along $\hat{y}$:[39]

$$H_D^{\mathrm{QW}i} = \frac{\hbar}{2}\vec{\sigma}\cdot\langle\vec{\Omega}(p)\rangle_y = \frac{\hbar\mathcal{C}}{2}\langle p_y^2\rangle[\sigma_x p_x - \sigma_z p_z] - \frac{\hbar\mathcal{C}}{2}\left[\sigma_x p_x p_z^2 - \sigma_z p_z p_x^2\right]. \tag{3}$$

The first term is linear in the in-plane momentum components (p_x,p_z), whereas the second term is cubic. Due to the strong confinement along $\hat{y}$ in our model, the cubic term can be ignored compared to the linear term:

$$H_D^{\mathrm{QW}i} \approx \frac{\hbar\mathcal{C}}{2}\langle p_y^2\rangle[\sigma_x p_x - \sigma_z p_z] \equiv \frac{\gamma_D}{\hbar}[\sigma_x p_x - \sigma_z p_z], \tag{4}$$

where γ_D represents the strength of the Dresselhaus spin-orbit coupling in the quantum wire system under consideration.

In presence of the $\hat{y}$ directed magnetic field as described before, the Dresselhaus Hamiltonian for the quantum wire will take the following form in the Landau gauge:

$$H_D^{\mathrm{QW}i,B} \approx \frac{\gamma_D}{\hbar}[\sigma_x(p_x + eBz) - \sigma_z p_z]. \tag{5}$$

Note that by varying $V_y(y)$ (and hence W_y), $\langle p_y^2\rangle$ can be changed, which will affect the strength of the Dresselhaus coupling γ_D. Such field-tunable Dresselhaus interaction is the basis of a new type of spin field-effect transistor as described in Ref. 4.

B. Perturbative approach and matrix elements

Combining Eqs. (1) and (5), the Pauli equation becomes

$$H\Psi(x,z) = E\Psi(x,z), \tag{6a}$$

$$H = \left[\frac{(p_x+eBz)^2}{2m^*} + \frac{p_z^2}{2m^*} + V_z(z)\right]\sigma_0 - \frac{g\mu_B\vec{B}\cdot\vec{\sigma}}{2} + \frac{\gamma_D}{\hbar}[\sigma_x(p_x+eBz) - \sigma_z p_z], \tag{6b}$$

where $\Psi(x,z)$ is the two-component eigenspinor corresponding to the energy eigenvalue E. Since the Hamiltonian in Eq. (6b) is independent of x, we take a plane-wave solution in this direction with wave number q_x, quantized in units of $2\pi/L$, where $L(\to\infty)$ is the length of the wire. The eigenspinor therefore takes the following form:

$$\Psi(x,z) = \frac{\exp(iq_x x)}{\sqrt{L}}\phi(z) \equiv \frac{\exp(iq_x x)}{\sqrt{L}}\begin{bmatrix}\phi^+(z)\\ \phi^-(z)\end{bmatrix}. \tag{7}$$

Using this solution, the Pauli equation can be transformed into the following form:

$$(H_0 + H_p)\phi(z) = \left(E - \frac{\hbar^2 q_x^2}{2m^*}\right)\phi(z) = \epsilon\phi(z), \tag{8a}$$

where $\epsilon = E - \frac{\hbar^2 q_x^2}{2m^*}$, the "unperturbed" part is chosen to be

$$H_0 = \left[-\frac{\hbar^2}{2m^*}\frac{d^2}{dz^2} + V(z)\right]\sigma_0 - \frac{g}{2}\mu_B B\sigma_y, \tag{8b}$$

and the remaining terms constitute the "perturbation" Hamiltonian

$$H_p = \left(\frac{e^2B^2z^2}{2m^*} + \frac{eBz\hbar q_x}{m^*}\right)\sigma_0 + \left(\gamma_D q_x + \frac{eBz\gamma_D}{\hbar}\right)\sigma_x + i\gamma_D\sigma_z\frac{d}{dz}. \tag{8c}$$

The exact solution of Eq. (8a) can be found numerically, which is presented in Sec. II C. However, it is instructive to examine the various coupling coefficients between the spin-split bands.

The set of eigenfunctions of H_0 are given by

$$\phi_0^{n',\sigma'} = \sqrt{\frac{2}{W_z}}\sin\left(\frac{n'\pi z}{W_z}\right)\zeta_{\sigma'} \quad \text{for } z\in[0,W_z],\ \zeta_\pm = \frac{1}{\sqrt{2}}\begin{bmatrix}1\\ \pm i\end{bmatrix} \tag{9a}$$

with the corresponding energy eigenvalues

$$\epsilon_0^{n',\sigma'} = \frac{\hbar^2}{2m^*}\left(\frac{n'\pi}{W_z}\right)^2 \mp \frac{g}{2}\mu_B B, \tag{9b}$$

where $\sigma'(\equiv\pm)$ indicates the spin-split levels. By expanding $\phi(z)$ in terms of the unperturbed eigenfunctions $\phi_0^{n',\sigma'}$, we obtain the following equations:

$$\phi(z) = \sum_{n',\sigma'} c_{n',\sigma'}\phi_0^{n',\sigma'}, \tag{10a}$$

$$\left(\epsilon_0^{n,\sigma} - \epsilon\right)c_{n,\sigma} + \sum_{n',\sigma'} c_{n',\sigma'}H_p^{nn',\sigma\sigma'} = 0, \sigma = \pm, \tag{10b}$$

$$H_p^{nn',\sigma\sigma'} = \left\langle\phi_0^{n,\sigma}\middle|H_p\middle|\phi_0^{n',\sigma'}\right\rangle, \tag{10c}$$

$$H_p^{nn',+-(-+)} = \frac{i[1-(-1)^{n+n'}]}{\pi}\frac{4nn'E_0}{(\Delta E(n,n')/E_0)}\sqrt{\frac{\Delta_{\mathrm{so}}^D}{E_0}} \times\left[1 \pm \frac{\hbar\omega_c}{E_0}\frac{E_0}{\Delta E(n,n')}\right], \quad \text{for } n\neq n', \tag{10d}$$

$$H_p^{nn,+-} = -H_p^{nn,-+} = -i\gamma_D\left(q_x + \frac{eBW_z}{2\hbar}\right) \equiv -i\gamma_D k_x, \tag{10e}$$

and

$$H_p^{nn',++} = H_p^{nn',--} = \frac{2nn'}{m^*W_z}\frac{(\hbar\omega_c/E_0)}{\left(\Delta E^2(n,n')/E_0^2\right)}\hbar^2 \times\left\{\frac{\hbar\omega_c}{E_0}\frac{\pi^3}{2W_z}(-1)^{n+n'} - q_x[1-(-1)^{n+n'}]\right\}, \tag{10f}$$

where

$$\Delta E(n,n') = \frac{\hbar^2}{2m^*}\left[\left(\frac{n\pi}{W_z}\right)^2 - \left(\frac{n'\pi}{W_z}\right)^2\right],$$

$$E_0 = \frac{\hbar^2\pi^2}{2m^*W_z^2}, \text{ and } \omega_c = eB/m^*.$$

We note that there are three relevant energy scales, namely, (a) energy gap between the subbands, which is

roughly characterized by $E_0 = \pi^2\hbar^2/2m^*W_z^2 \approx 1.255$ meV for the lower order bands, (b) Dresselhaus spin-orbit coupling strength represented by $\Delta_{so}^D = m^*\gamma_D^2/2\hbar^2 \approx 0.02$ meV for $\gamma_D = 10^{-11}$ eVm,[14,34] and (c) Landau energy $\hbar\omega_c = e\hbar B/m^* \approx 3.86$ meV for $B = 1$ T. The relative strengths of these energies, controllable by γ_D and B, determine the subband structure and profoundly affect the spin texturing. We note that a factor of two reduction in W_y results in a factor of 16 increase in Δ_{so}^D.

The terms $H_p^{nn',+-}$ and $H_p^{nn',-+}(n \neq n')$ in Eq. (10d) indicate coupling between opposite spin states $(+,-)$ belonging to different $(n \neq n')$ subbands, whereas the terms $H_p^{nn,+-}$ and $H_p^{nn,-+}$ in Eq. (10e) represent coupling between the spin-split branches of the same subband. The terms $H_p^{nn',++}$ and $H_p^{nn',--}$ in Eq. (10f) are coupling between same spin states belonging to different subbands. From the above equations, the following observations can be made:

(1) we note that in absence of the spin-orbit interaction ($\gamma_D = 0$) coupling between the opposite spin states is zero. This makes intuitive sense since in the absence of spin-orbit coupling, the only spin-dependent term is the Zeeman term, which results in spin eigenstates $\zeta_\pm$ [see Eq. (9a)]. Clearly such states are decoupled in absence of other spin-dependent terms.

(2) On the other hand, coupling between same spin states exist even in absence of spin-orbit interaction. This is due to the first term in the perturbation Hamiltonian [see Eq. (8c)], which effectively modifies the potential profile in the range $[0, W_z]$.

(3) The coupling between the Zeeman split states in a given subband depends only on the spin-orbit coupling strength γ_D and the shifted wave vector k_x. This is in stark contrast with the parabolic confinement case,[31] where the analogous term also depends on the parabolic confinement and vanishes in the 2D limit.

C. Numerical approach

For numerical calculation of the energy eigenvalues E and the (spinor) eigenfunctions $\phi(z)$ of the Hamiltonian in Eq. (8a), we use the following method. Equation (8a) can be recast into the following form:

$$\left[\mathbf{B}q_x + \mathbf{C} - \mathbf{A}q_x^2\right]_{2\times2}\phi(z)_{2\times1} = E\phi(z)_{2\times1}, \tag{11}$$

where

$$\mathbf{A} = -\frac{\hbar^2}{2m^*}\sigma_0, \tag{12a}$$

$$\mathbf{B} = \frac{eB\hbar z}{m^*}\sigma_0 + \gamma_D\sigma_x, \tag{12b}$$

$$\mathbf{C} = \left[-\frac{\hbar^2}{2m^*}\frac{d^2}{dz^2} + V_z(z) + \frac{e^2B^2z^2}{2m^*}\right]\sigma_0 - \frac{g\mu_B B\sigma_y}{2} + \frac{\gamma_D}{\hbar}\left(eBz\sigma_x + i\hbar\sigma_z\frac{d}{dz}\right). \tag{12c}$$

Equation (11) is solved numerically for each q_x (or k_x) to find the eigenvalue E and the corresponding eigenfunction $\phi(k_x,z)$ subject to the boundary conditions $\phi^{\pm}(k_x,z) = 0$ for $z = 0, W_z$. A similar numerical model has been used in Refs. 14–16.

III. RESULTS AND DISCUSSION

Spin texture is known to depend critically on the subband structure.[15] Magnetoelectric subbands that form in quantum confined systems in presence of spin-orbit interaction have been studied by many groups in the past.[12,13,18,30–32,34] All of these studies have chosen a parabolic confinement potential and therefore the results from these work cannot directly be applied in the present case where the confinement is hard-wall type. Therefore we first briefly highlight the essential features of the magnetoelectric subbands that arise for hard-wall confinement.

A. Energy spectrum

1. Without spin-orbit interaction ($\gamma_D = 0$)

We first consider the simple case when the Dresselhaus spin-orbit interaction is zero but the external magnetic field is present. In this case, coupling between opposite spin states will vanish ($H_p^{nn',\sigma\sigma'} = 0, \sigma \neq \sigma'$) as can be seen from Eqs. (10d) and (10e). The magnetic field makes the potential profile parabolic in the range $[0, W_z]$ and enhances the confinement [first term in Eq. (8c)] by an amount $\frac{1}{2}m^*\omega_c^2 z(z + 2z_0)$, where $z_0 = \frac{\hbar q_x}{eB}$. As a result, the subband bottoms are shifted vertically upward compared to the $B = 0$ case as shown in Figs. 2(a) and 2(b). Additionally, each subband is Zeeman split due to the magnetic field.

Figure 2(a) shows the magnetoelectric subbands for $B =$ 1T (or $\hbar\omega_c/E_0 = 3$). The subband bottoms are more flat compared to the parabolic ($B = 0$) case and the flatness increases with increasing B [see Fig. 2(b), $B = 2$T, $\hbar\omega_c/E_0 =$ 6] indicating the formation of closed Landau orbits.

2. Without external magnetic field ($B = 0$)

To identify the effect of the Dresselhaus spin-orbit interaction on the subband structure, we first consider the case when the external ($\hat{y}$ directed) magnetic field is absent. We vary the Dresselhaus parameter γ_D in a wide range that can be divided in three distinct categories: (a) weak spin-orbit limit, characterized by $\Delta_{so}^D/E_0 \leqslant 0.1$, (b) strong spin-orbit interaction for which $\Delta_{so}^D/E_0 \approx 1$, and (c) the giant spin-orbit limit, which represents the situation $\Delta_{so}^D/E_0 >> 1$. As mentioned before, γ_D can be changed by varying the confinement (W_y) along $\hat{y}$. Figures 3(a)–3(e) show the magnetoelectric subbands for these three cases. In Fig. 3(a), the weak spin-orbit interaction lifts the spin degeneracy at all points except $k_x = 0$ and generates two horizontally displaced parabolas, which are uniformly shifted downward compared to the spin-degenerate band. These features have been reported earlier by several groups in the context of parabolic confinement[31–34] and can be understood simply as follows.

In the absence of the external magnetic field, the term $H_p^{nn',\sigma\sigma}(n \neq n')$ is zero and if we ignore intersubband coupling [i.e., $\Delta E(n,n') \to \infty$] then the term $H_p^{nn',\sigma\sigma'} \propto nn'/\Delta E(n,n'), (n \neq n', \sigma \neq \sigma')$ vanishes as well, irrespective of the value of spin-orbit interaction strength Δ_{so}^D/E_0. In this case, the only surviving term is $H_p^{nn,+-} = -H_p^{nn,-+} =$

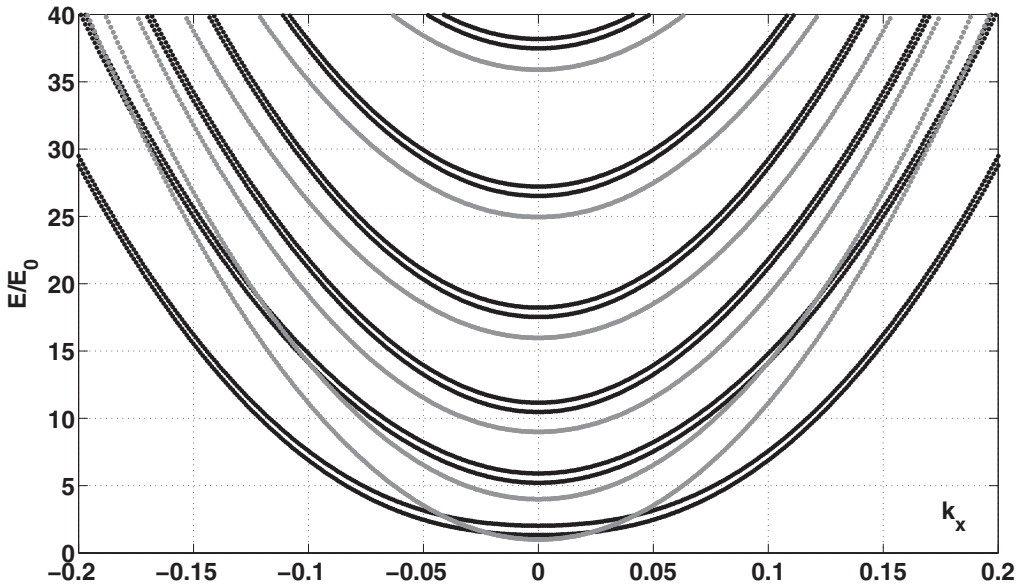

(a)

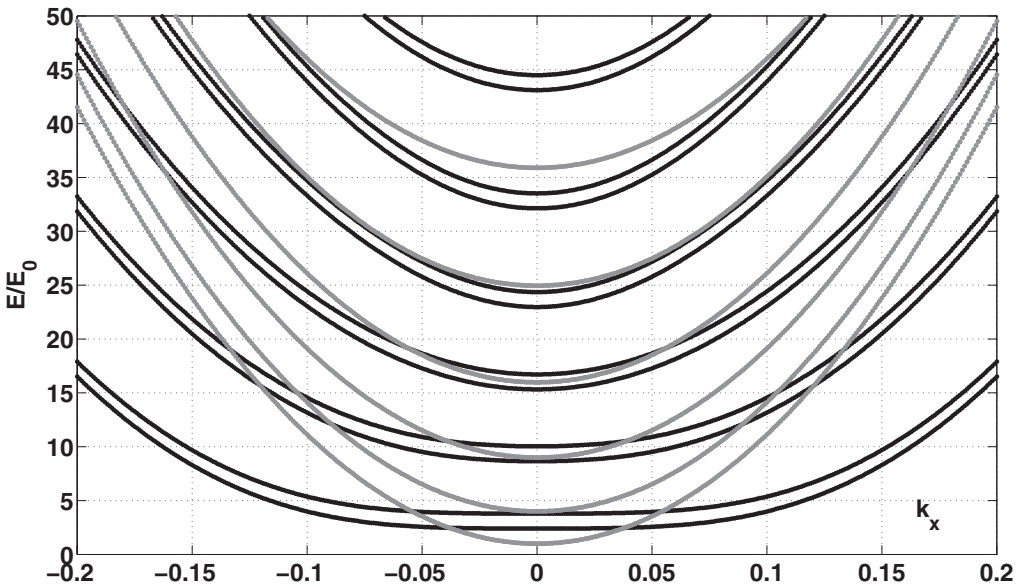

(b)

FIG. 2. Magnetoelectric subbands in absence of spin-orbit interaction ($\gamma_D = 0$). The grey curves represent the spin-degenerate subbands, which occur when the magnetic field is also zero. The dark curves indicate the Zeeman-split subbands for (a) magnetic field $B = 1$ T ($\hbar\omega_c/E_0 = 3$) and (b) $B = 2$ T ($\hbar\omega_c/E_0 = 6$). The shifted wave vector k_x is in nm^{-1}.

$-i\gamma_D k_x$. It is then straightforward to directly calculate the energy eigenvalues from Eq. (10b), which gives

$$E = \frac{\hbar^2}{2m^*}\left(k_x \pm \frac{m^*\gamma_D}{\hbar^2}\right)^2 + E_{00},$$

where

$$E_{00} = \left[\frac{\hbar^2}{2m^*}\left(\frac{n\pi}{W_z}\right)^2 - \frac{m^*\gamma_D^2}{2\hbar^2}\right].$$

Clearly, compared to the zero γ_D case, the spin-split bands have shifted horizontally by an amount $\pm m^*\gamma_D/\hbar^2$ and vertically downward by an amount $m^*\gamma_D^2/2\hbar^2$. This feature is clearly seen in Figs. 3(a) and 3(b). This model also indicates that the parabolicity of all bands is maintained, irrespective of the value of γ_D. However, nonparabolicity is quite apparent in Figs. 3(c)–3(e), which we discuss next.

Figure 3(c) shows the subband structure for strong spin-orbit coupling ($\Delta_{so}^D/E_0 = 1$). The degeneracy at $k_x = 0$ is maintained. Deviation from nonparabolicity is accentuated for higher spin-orbit coupling (Δ_{so}^D/E_0) strengths, as shown in Figs. 3(c), 3(d), and 3(e). This is because of finite intersubband coupling ($H_p^{nn',\sigma\sigma'} \neq 0, \sigma \neq \sigma'$), the strength of which increases with $\sqrt{\Delta_{so}^D/E_0}$ [see Eq. (10d)].

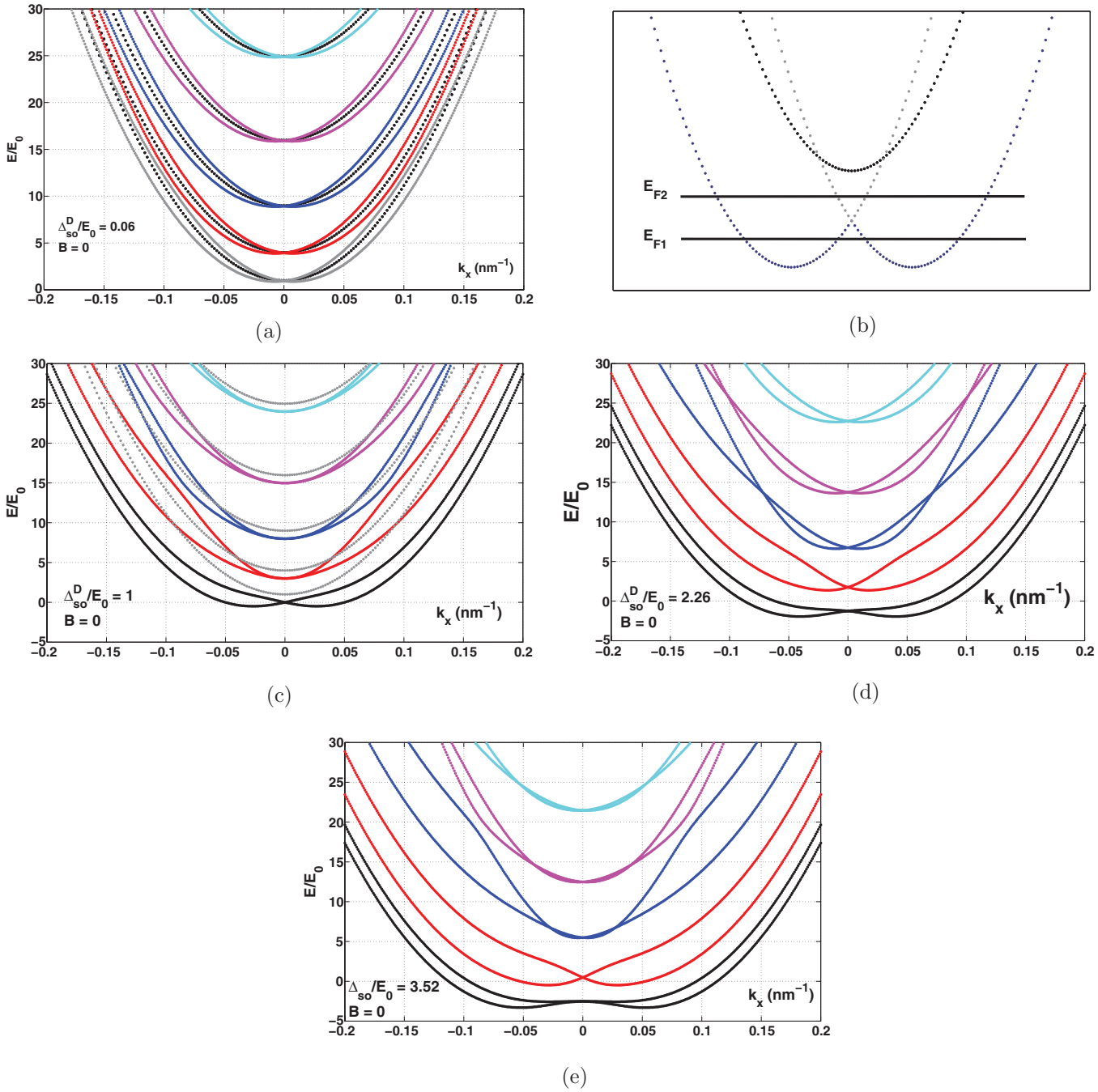

FIG. 3. (Color online) Energy spectrum in presence of finite Dresselhaus spin-orbit interaction and zero magnetic field. Subband structure in (a) the weak spin-orbit (Dresselhaus) regime, i.e., $\Delta_{so}^{D}/E_0 < 0.1$, and (b) magnified region near $k_x = 0$ for the lowest subband in (a). The horizontal lines (E_{F1}, E_{F2}) represent two possible locations of the Fermi level. The upper parabola corresponds to the spin-degenerate case (no spin-orbit interaction), (c) the strong spin-orbit (Dresselhaus) regime, i.e., $\Delta_{so}^{D}/E_0 = 1$, and (d) and (e) giant spin-orbit (Dresselhaus) regime, i.e., $\Delta_{so}^{D}/E_0 >> 1$. The dotted lines in (a) and (c) indicate the spin-degenerate subband structure in absence of Dresselhaus spin-orbit interaction.

3. Simultaneous presence of spin-orbit interaction and magnetic field ($\gamma_D \neq 0, B \neq 0$)

Next, let us consider the case when both spin-orbit interaction and magnetic field are present. Figures 4(a)–4(e) show representative situations. In these plots, we keep the spin-orbit coupling fixed at the "strong limit" (i.e., $\Delta_{so}^{D}/E_0 = 1$) and vary the magnetic field from weak [$\hbar\omega_c/E_0 = 0.1$, Figs. 4(a) and 4(b)] to strong [$\hbar\omega_c/E_0 \approx 1$, Fig. 4(c)] and finally, giant [$\hbar\omega_c/E_0 = 10$, Figs. 4(d) and 4(e)] limit. Due to the presence of the magnetic field, spin degeneracy is lifted at all k_x. In the strong and giant B limit, the term $H_p^{nn',\sigma\sigma},\sigma = \pm$ [see Eq. (10f)] dominates and the subband structure [see Figs. 4(d) and 4(e)] approximately resembles those of Fig. 2(b). However, unlike Fig. 2(b), due to the presence of the spin-orbit term, the spin splitting is k_x dependent. The effect of spin-orbit term is more prominent in the weak B limit [see Fig. 4(a)],

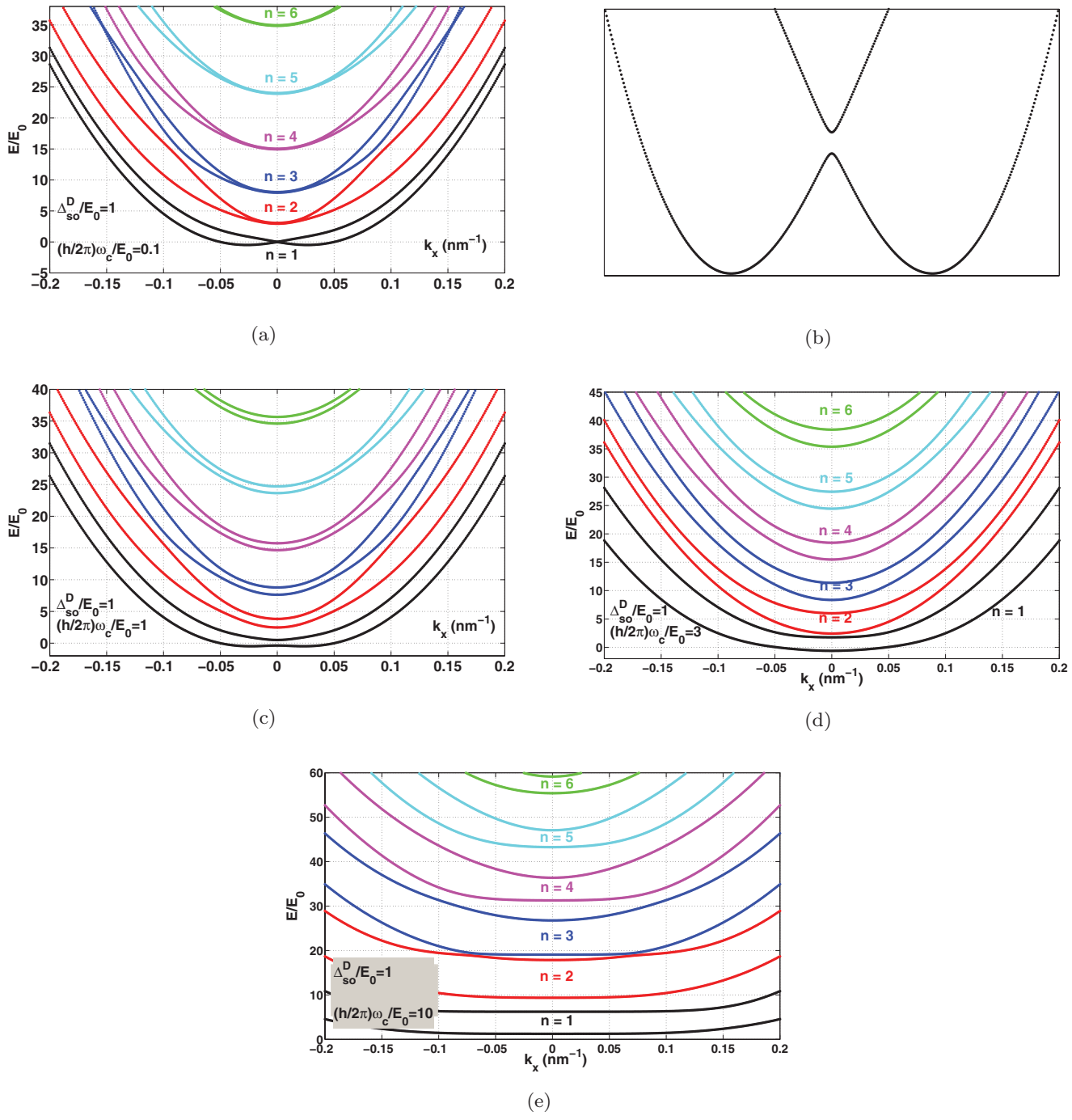

FIG. 4. (Color online) Energy spectrum in presence of strong Dresselhaus spin-orbit interaction ($\Delta^D_{so}/E_0 = 1$) and an external magnetic field. (a) Weak magnetic field limit ($\hbar\omega_c/E_0 = 0.1$), (b) magnified image of subband 1 in (a) near $k_x = 0$, showing the camelback feature, (c) strong ($\hbar\omega_c/E_0 = 1$), and (d) and (e) giant ($\hbar\omega_c/E_0 >> 1$) magnetic field regime.

where the lowest spin-split band has a "Mexican hat" (or "camelback")[40] shape. This feature is also present in Rashba spin-orbit systems in presence of axial[41] or transverse[15] magnetic field. This is a signature of spin-orbit coupling and gradually disappears as the external magnetic field is increased as shown in Figs. 4(a)–4(e).

The critical magnetic field (B_c) for which the camelback shape disappears has been estimated[40] under the assumption of negligible intersubband coupling:

$$B_c = \frac{2m^*\gamma_D^2}{|g|\mu_B\hbar^2}.$$

Clearly, this estimate is only valid in the small spin-orbit limit where the intersubband coupling is negligible. In the strong spin-orbit limit [as in Figs. 4(a)–4(c)], the estimated value of B_c using the above formula is 0.174 T, whereas the camelback

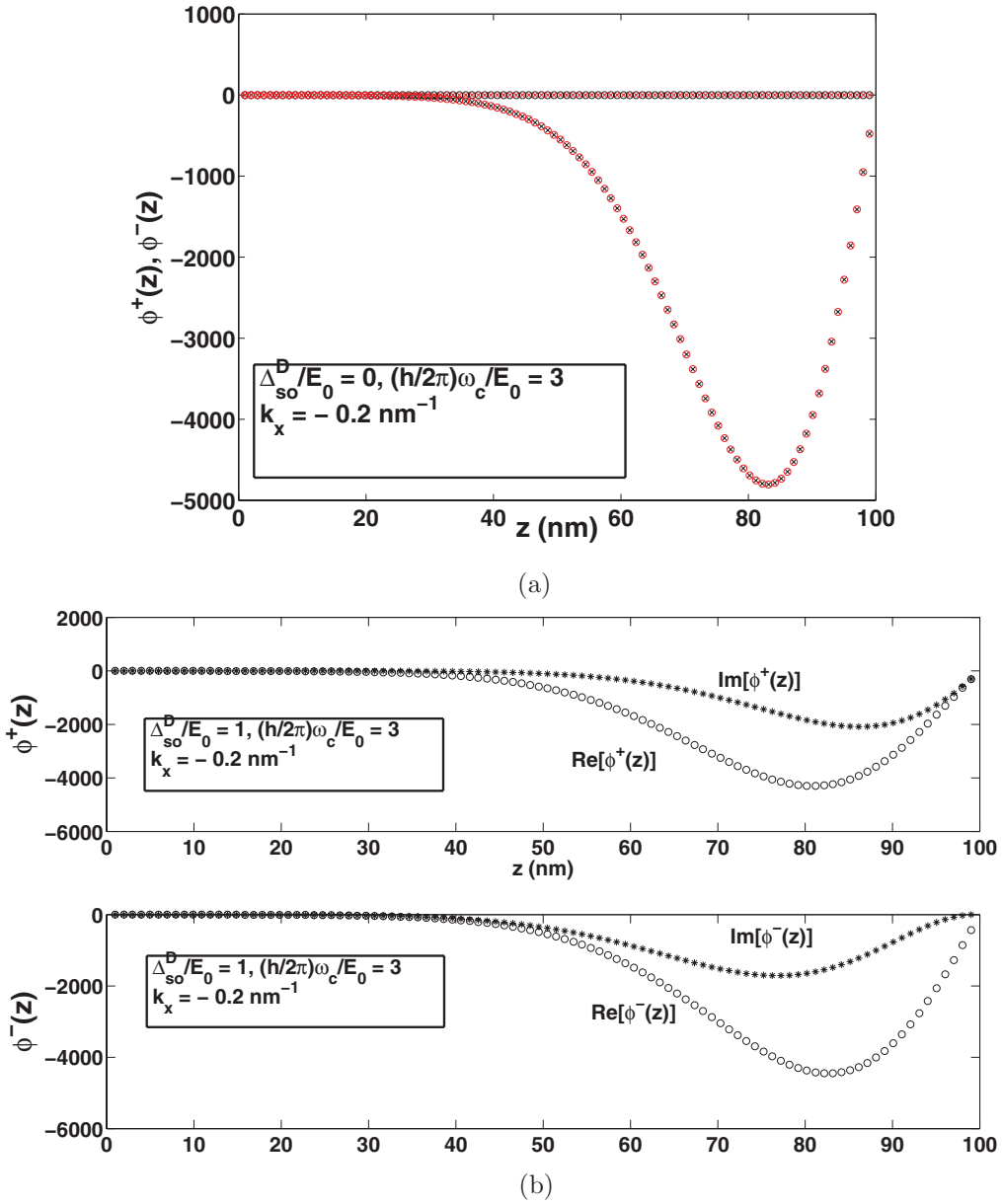

FIG. 5. (Color online) Edge states in a quantum wire in giant magnetic field limit ($\hbar\omega_c/E_0 = 3$): (a) in absence of spin-orbit interaction ($\Delta^D_{so}/E_0 = 0$) and (b) with *strong* spin-orbit interaction ($\Delta^D_{so}/E_0 = 1$). The z dependence of the real (denoted by "o") and imaginary (denoted by "*") parts of the spinor wave function $\phi(z) = [\phi^+(z)\ \phi^-(z)]^T$ are shown. In (a), black symbols indicate $\phi^+(z)$ and the red symbols indicate $\phi^-(z)$. All plots correspond to the wave vector $k_x = -0.2\ \text{nm}^{-1}$ and the lowest Zeeman-split branch of subband 1.

shape persists at higher magnetic fields [see Fig. 4(c), $B =$ 0.33 T]. The camelback shape is less prominent for higher subbands.

B. Wave functions

Figure 5 shows the typical spinor wave functions $\phi^+(k_x,z)$ and $\phi^-(k_x,z)$ for subband 1 in presence of giant magnetic field ($\hbar\omega_c/E_0 = 3$) for two different cases: (a) in absence of Dresselhaus spin-orbit coupling [$\Delta^D_{so}/E_0 = 0$, Fig. 5(a)] and 5(b) with strong spin-orbit coupling [$\Delta^D_{so}/E_0 = 1$, Fig. 5]. In both cases, we show the wave function corresponding to the lowest spin-split band ($n = 1$) with $k_x = -0.2\ \text{nm}^{-1}$. The wave function is skewed to the right edge of the quantum wire, because of the $+\hat{z}$ directed Lorentz force acting on the backward traveling electrons.

From Fig. 5(a), we note that the spinor wave function $\phi(k_x,z) = [\phi^+(k_x,z)\ \phi^-(k_x,z)]^T$ can be separated in a spatial part $\phi^s(k_x,z)$ and a space-independent spinor part $[i\ 1]^T$. Clearly the spinor part is the eigenfuntion of σ_y corresponding to the eigenvalue -1 as expected for the lowest spin-split band with a negative g factor [see Eq. (6b)].

However, this situation changes completely in presence of spin-orbit interaction. In Fig. 5(b), we show the wave functions for strong spin-orbit interaction $\Delta^D_{so}/E_0 = 1$. Note that now it is not possible to separate the spatial part and the spinor part of the wave function and hence the two-component spinor wave function cannot be expressed as a product of

a space-dependent function and a space-independent spinor part. Similar observation has been made in previous works such as Refs. 12,13,16, and 17. In the following section, we will show how this feature gives rise to spin texture along the transverse width of the quantum wire.

C. Spin textures

The spin orientation of the eigenspinor $\phi_n(k_x,z)$ in the nth subband [see Eq. (8a)] is given by[20]

$$\vec{\tilde{\sigma}}_n(k_x,z) = \phi_n^{\dagger}(k_x,z)\,\vec{\sigma}\,\phi_n(k_x,z). \tag{13}$$

The corresponding spin "density" for a given k_x is defined as[15]

$$\vec{s}^n(k_x,z) = \frac{\vec{\tilde{\sigma}}_n(k_x,z)}{|\vec{\tilde{\sigma}}_n(k_x,z)|}. \tag{14}$$

To compute the real-space spin density $\vec{S}(z)$ (or spin texture) that can be probed experimentally, we combine the spin density contribution from all occupied states:[15,20,22]

$$\vec{S}(z) = \sum_{n=1}^{N} \frac{\int_{k_{Fn}^-}^{k_{Fn}^+} \vec{s}^n(k_x,z)dk_x}{k_{Fn}^+ - k_{Fn}^-}, \tag{15}$$

where N is the number of occupied spin-split levels and $k_{Fn}^+(k_{Fn}^-)$ is the wave vector of the nth level where the Fermi level intersects the $E-k_x$ plot on the right (left) of the energy axis. Here, we assume that the temperature is low enough such that the states below the Fermi level are fully occupied whereas those above it are unoccupied.

Equation (15) can be applied directly when the Fermi level intersects the subband only at two points, one on each side of the energy axis. However, under certain situations, Fermi level can intersect the same band at four different points. For example, in Fig. 4(b), if the Fermi level is below the local energy maxima at $k_x = 0$, then it intersects the lower subband at four different points. In such case, Eq. (15) is modified as follows:[15]

$$\vec{S}(z) = \frac{\int_{k_{F1}}^{k_{F2}} \vec{s}^n(k_x,z)dk_x}{k_{F2}-k_{F1}} + \frac{\int_{k_{F1'}}^{k_{F2'}} \vec{s}^n(k_x,z)dk_x}{k_{F2'}-k_{F1'}}, \tag{16}$$

where $k_{F1},k_{F2}(k_{F1'},k_{F2'})$ are the wave vectors where the Fermi level intersects the lowest spin-split band on the left (right) of the energy axis.

A similar situation arises in $B=0$ case where the spin-split subbands are displaced horizontally. If the Fermi energy is below the degeneracy point (at $k_x = 0$) of subband 1, then we can again use Eq. (16), but $k_{F1},k_{F2}(k_{F1'},k_{F2'})$ will then indicate the intersection points of the left (right) shifted band with the Fermi level.

We note that z dependence of $\vec{s}^n$ (and hence $\vec{S}$) originates from the fact that in presence of spin-orbit interaction, the spinor wave function cannot be separated into a space-dependent part and a space-independent spinor component as discussed in the previous section [see Fig. 5(b)]. The spin texture, i.e., spatial modulation of $\vec{S}$ along z, is therefore critically dependent on the wave functions in presence of spin-orbit coupling. In the following discussion, we will discuss the spatial evolution of $\vec{S}(z)$ for a wide range of magnetic fields and Dresselhaus spin-orbit interaction strengths.

1. Without spin-orbit interaction ($\gamma_D = 0$)

We start with the simple case when the spin-orbit interaction is absent ($\Delta_{so}^D/E_0 = 0$) and the wire is subjected to a moderate external magnetic field ($\hbar\omega_c/E_0 = 0.3$). In this case, the band structure resembles Figs. 2(a) and 2(b), and each subband will be split vertically into two branches. Since $B\hat{y}$ is the sole magnetic field present in the system, only $\hat{y}$ component [$S_y(z)$] of $\vec{S}(z)$ will be nonzero and other components will vanish. Since B is independent of the spatial coordinates, $S_y(z)$ will be independent of z. Further, $S_y(z)$ will be negative if the lowest Zeeman-split band is considered since the g factor is negative in Eq. (1). Such a situation is depicted in Fig. 6(a).

If both lower and upper Zeeman-split bands are occupied [see Fig. 6(b)], then the overall $|S_y(z)|$ is significantly lower due to the averaging effect as described by Eq. (15). In this case, the upper Zeeman branch has spins along $+\hat{y}$, which partially cancel the spins of the lower branch, which are oriented along $-\hat{y}$.

From Figs. 6(a) and 6(b), we note that in absence of spin-orbit interaction, components of $\vec{S}(z)$ are independent of the transverse coordinate z and hence no spin "texturing" or spatial modulation of spin density exists.

2. Without external magnetic field (B=0)

We next consider another limiting case when the external magnetic field is zero ($\hbar\omega_c/E_0 = 0$) but the Dresselhaus spin-orbit interaction is present ($\Delta_{so}^D/E_0 = 0.06$). In this case, the band structure resembles Figs. 3(a) and 3(b) where the spin-orbit coupling splits the spin-degenerate band into two horizontally displaced branches, which are degenerate only at $k_x = 0$. Such zero-field spin splitting has been used before to define a k_x-dependent effective Dresselhaus spin-orbit magnetic field $\vec{B}_D$ acting along $\pm\hat{x}$.[17,40]

Since in this case there is no net $\hat{y}$- or $\hat{z}$-directed magnetic field, the components of $\vec{S}(z)$ along these directions are zero. Additionally, since the sample is overall nonmagnetic, $S_x(z)$ will be zero as well for any z. This is shown in Fig. 6(c). Another physical explanation is provided below.

3. Simultaneous presence of spin-orbit interaction and magnetic field ($\gamma_D \neq 0, B \neq 0$)

In this case, due to the presence of both $\hat{x}$- and $\hat{y}$-directed magnetic fields, components of $\vec{S}(z)$ are nonzero along these directions and lie in the xy plane. Their exact orientation will depend on the relative values of the quantities Δ_{so}^D/E_0 and $\hbar\omega_c/E_0$, which represent the strengths of spin-orbit interaction and the applied magnetic field, respectively. Since there is no net $\hat{z}$-directed magnetic field in any situation, the z component of $\vec{S}(z)$ is zero at all locations and hence the spin vector $\vec{S}(z)$ is two dimensional.

Small carrier concentration. We first consider the case when the carrier concentration is "small" so that only the lowest spin-split band is occupied at zero Kelvin (the Fermi level is below the bottom of the upper spin-split level of subband 1). Figure 7 shows the spin texture in real space for a weak Dresselhaus spin-orbit coupling strength ($\Delta_{so}^D/E_0 = 0.06$) and an external magnetic field varying from the weak to the giant limit ($\hbar\omega_c/E_0 = 0.006$–$6$). Figure 8 shows the texture

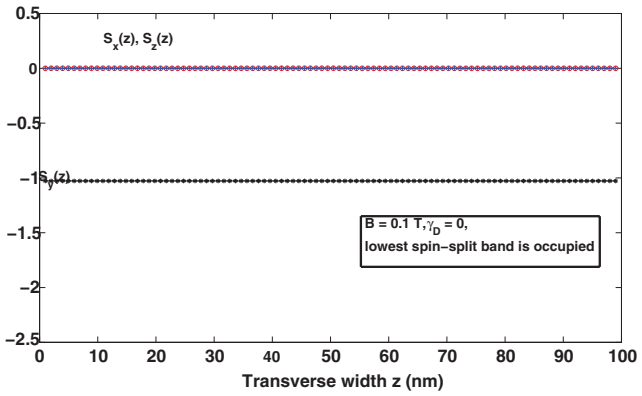

(a)

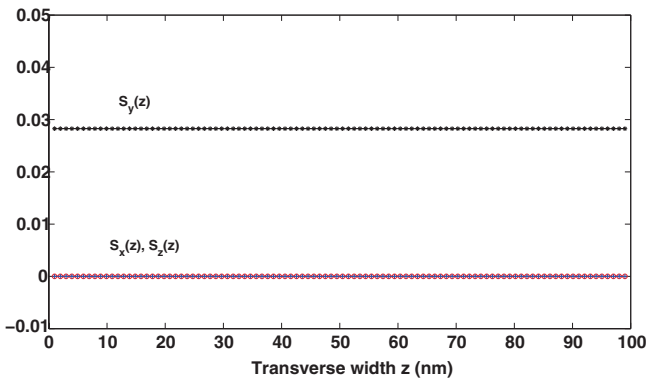

(b)

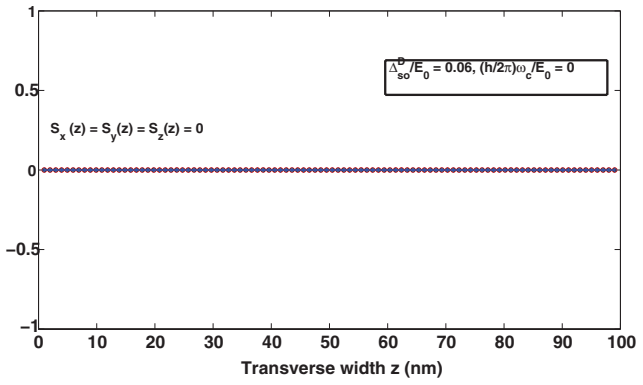

(c)

FIG. 6. (Color online) Components of $\vec{S}(z)$ along the width of the quantum wire. (a) and (b) $\gamma_D = 0$ ($\Delta^D_{so}/E_0 = 0$) and $B = 0.1$T ($\hbar\omega_c/E_0 = 0.3$). (a) Only the lowest spin-split band of subband 1 is occupied. (b) Both spin-split bands of subband 1 are occupied. (c) $\gamma_D \neq 0$ ($\Delta^D_{so}/E_0 = 0.06$), $B = 0$ ($\hbar\omega_c/E_0 = 0$), and the lowest subband is occupied. In (c), all components of $\vec{S}(z)$ are zero since the sample is nonmagnetic and no external field is present.

for the strong ($\Delta^D_{so}/E_0 = 1$) and the giant ($\Delta^D_{so}/E_0 >> 1$) spin-orbit limits.

For Figs. 7(a)–7(e), 8(a), 8(b), and 8(d), the magnetic field is below the critical value and therefore the lowest spin-split band has a camelback structure. The Fermi level can be either above [e.g., Figs. 7(b), 7(d), 7(e), 8(a), 8(b), and 8(d)] or below [see Figs. 7(a) and 7(c)] the local maximum at $E(k_x = 0)$. For Figs. 7(f), 8(c), 8(e), and 8(f), the camelback feature is not present.

The spin textures in all these cases have certain features in common.

(1) The $\hat{x}$ component of $\vec{S}(z)$ is zero at the wire center and takes positive (negative) values for $z < W_z/2$ ($z > W_z/2$), i.e., it has a negative slope in the vicinity of $z = W_z/2$. For the large spin-orbit case ($\Delta^D_{so}/E_0 \geqslant 1$, Fig. 8) S_x attains an extremum near the edges. In all cases, S_x has opposite signs at the two edges.

The features in Figs. 6(c) and 7 can be qualitatively understood as follows. The electrons in the quantum wire experience two magnetic fields: (a) the external, space-invariant magnetic field $B\hat{y}$ and (b) the pseudomagnetic field due to the Dresselhaus spin-orbit coupling (say $\vec{B}_D$). This pseudomagnetic field can be estimated in two different ways.[17,40] However, in the present case, we are interested in estimating the $\vec{B}_D$ experienced by an electron with a given k_x. For this purpose, we equate the "effective" Zeeman splitting energy due to $\vec{B}_D$ to the spin-splitting energy $\gamma_D k_x$, which yields $\vec{B}_D = \gamma_D \vec{k}_x/|g|\mu_B$.[26,29] Clearly, this field is dependent on the electron wave vector k_x and is oriented along the wire axis ($\pm\hat{x}$).

Electrons with positive k_x will experience a $+\hat{x}$-directed $\vec{B}_D$. Now, if these electrons belong to the lower (upper) spin-split band, their spins will orient along $+(-)\hat{x}$ since the wire material has a negative g factor. Using the same argument, electrons with negative k_x will experience a $-\hat{x}$-directed $\vec{B}_D$. Again, if these electrons belong to the lower (upper) spin-split subband, their spins will orient along $-(+)\hat{x}$, due to the negative g factor of the wire material. The states with zero k_x experience no Dresselhaus magnetic field. This is expected, since by definition, spin-orbit interaction is present only for moving electrons and no spin-orbit-induced splitting is present for zero k_x.

If no other magnetic field (spin-orbit related or externally applied) is present as in Fig. 6(c), then the spin polarizations will be purely along $\pm\hat{x}$. Under equilibrium and when no external magnetic field is present, $+k_x$ and k_x states will cancel each other at any location z, resulting in zero current. At the same time, since their spins are oppositely oriented, the total

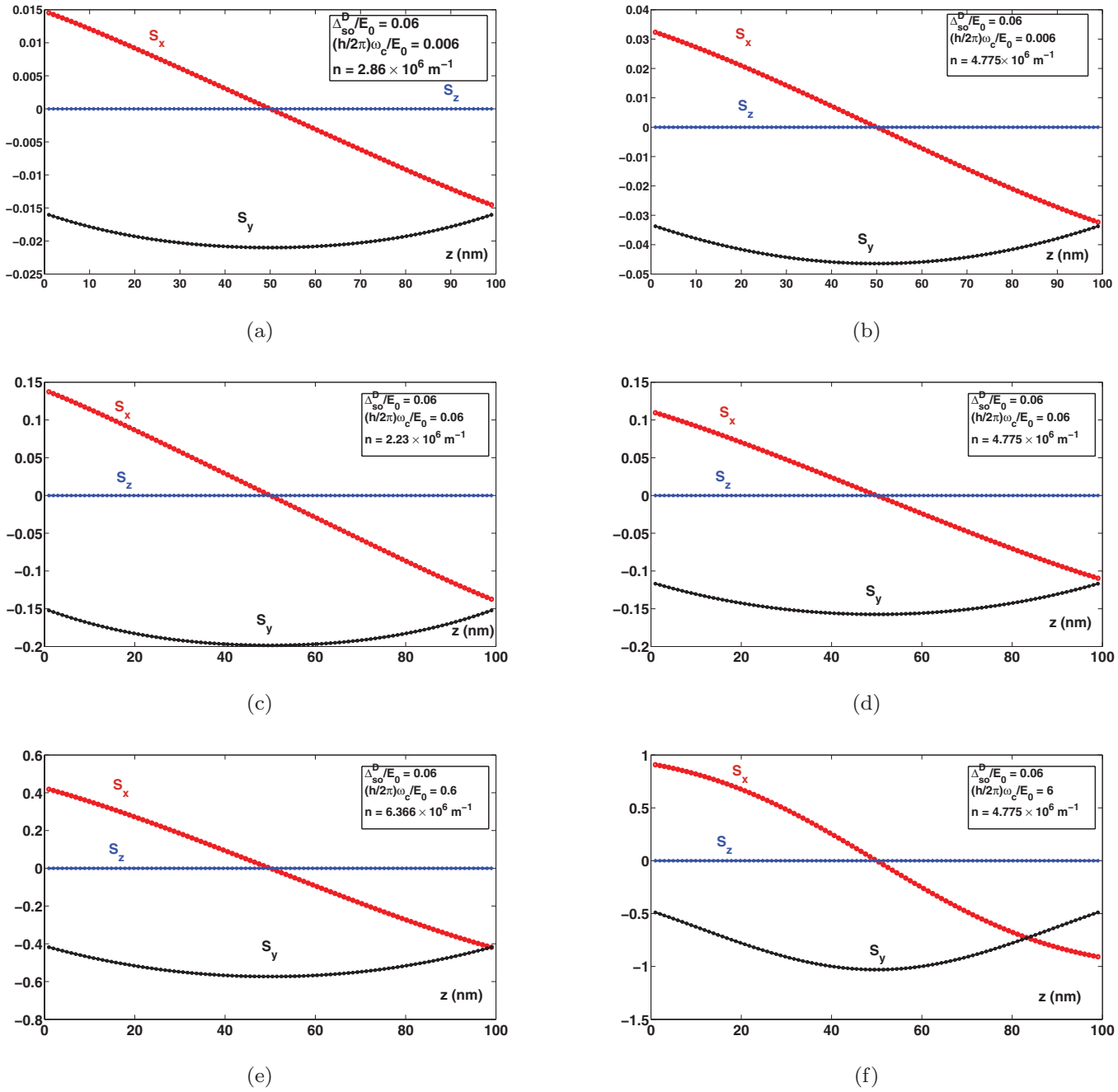

FIG. 7. (Color online) Spin texture for the weak spin-orbit coupling case ($\Delta_{so}^{D}/E_0 = 0.06$) and lowest spin-split subband occupancy for various carrier concentrations. Magnetic field is varied from the weak [$\hbar\omega_c/E_0 = 0.006$ in (a) and (b)] to the moderate [$\hbar\omega_c/E_0 = 0.06$ in (c) and (d)], the strong [$\hbar\omega_c/E_0 = 0.6$ in (e)], and the giant [$\hbar\omega_c/E_0 = 6$ in (f)] limits. Except (f), in all cases, the lowest spin-split subband has a camelback shape. In (a) and (c), E_F is below the local maximum at $E(k_x = 0)$, whereas in (b), (d), and (e), E_F is above this value but below the bottom of the upper spin-split band of subband 1.

spin component along $\hat{x}$ will be zero. Therefore no net spin component is observed when the external magnetic field is zero and the system is in equilibrium. As mentioned before, this physical picture is consistent with the fact that the quantum wire is nonmagnetic and agrees with Fig. 6(c).

When an external magnetic field is applied along $+\hat{y}$, positive and negative k_x states are spatially separated along z (see Fig. 5). Due to Lorentz force, electrons with positive k_x will deflect toward $z = 0$, whereas electrons with negative k_x will shift toward $z = W_z$. Therefore now one expects a net $+\hat{x}$ component of spins near $z = 0$ and a net $-\hat{x}$ component of spins near $z = W_z$ for the states belonging to the lowest spin-split band. The sign of the $\hat{x}$ component of spin polarization at the two edges will change if the upper spin-split band is considered. States with zero k_x will remain at the center ($z = W_z/2$) and will show a net zero $\hat{x}$ component of spin at this location. As a result a spatial variation in the net $\hat{x}$ component of spin is observed (see Fig. 7).

(2) The external magnetic field will also orient the spins along $-(+)\hat{y}$ for the lower (upper) spin-split band as evident from the Zeeman term in our model [see Eq. (6b)]. The net magnetic field is entirely $\hat{y}$ directed at the center because electrons in that region experience zero $\vec{B}_D$ as described before. Therefore the $\hat{y}$ component of spin has the largest magnitude at the center. As we move away from the center, the magnitude of $\vec{B}_D$ increases and the net magnetic field gradually accumulates an $\hat{x}$ component. As a result, the magnitude of $\hat{y}$ component of spin gradually reduces toward the edges, whereas the magnitude of $\hat{x}$ component of spin increases. This qualitatively explains the spatial textures of the net spin components and the $\pi/2$ phase shift between them.

The physical picture outlined above is consistent with our numerical simulation, which shows $S_x(z) > 0 (< 0)$ for $z > W_z/2 (< W_z/2)$ and $S_y(z) > 0$ for the electrons in a lower spin-split band for a positive g factor material. As expected, opposite signs have been observed for the electrons in a upper spin-split band.

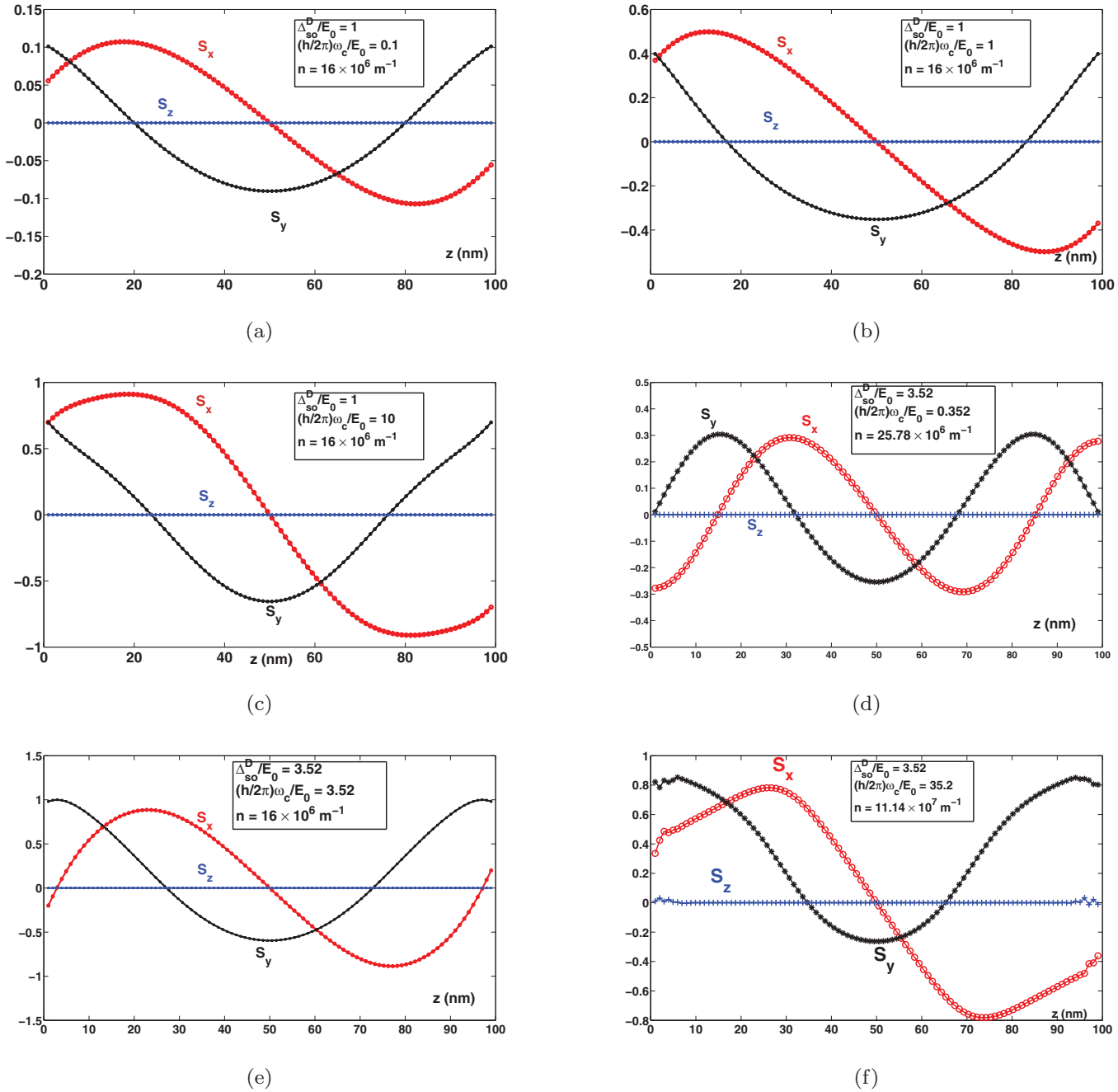

FIG. 8. (Color online) Spin texture for the strong [$\Delta^D_{so}/E_0 = 1$ in (a)–(c)] and the giant [$\Delta^D_{so}/E_0 = 3.52$ in (d)–(f)] spin-orbit couplings. Magnetic field is varied from the weak to the strong limit [$\hbar\omega_c/E_0 = 0.1$–10 in (a)–(c) and $\hbar\omega_c/E_0 = 0.352$–$35.2$ in (d)–(f)]. The lowest spin-split band is occupied in all cases. For (a), (b), and (d), the lowest band has the camelback shape and the Fermi level is above $E(k_x = 0)$.

(3) Stronger spin-orbit interaction shortens the "wavelength" of the standing wave of the spin components as can be seen from Fig. 8. Interestingly, even in the strong B limit [$\hbar\omega_c/E_0 >> \Delta_{so}^D/E_0$, Figs. 7(e) and 7(f)], we find a strong $\hat{x}$ component to persist. This can be attributed to B dependence of B_D via the k_x term. This feature is in stark contrast with the Rashba case reported in Ref. 15, where a strong external magnetic field ($B\hat{y}$) masks the weaker Rashba field and rotates the spins predominantly along $\hat{y}$.

Large carrier concentration. We now consider the case when the carrier concentration is "large" enough so that both spin-split branches of the lowest subband are occupied. Figure 9(a) shows the spin texture for the case when both spin-orbit interaction and magnetic field are weak (i.e., $\Delta_{so}^D/E_0 = 0.06$,$\hbar\omega_c/E_0 = 0.006$). Figure 9(b) shows the spin texture for each spin-split branch of the lowest subband 1 and the net spin components. For this case, both spin-orbit coupling and magnetic field are weak ($\Delta_{so}^D/E_0 = 0.06$, $\hbar\omega_c/E_0 = 0.1$). Figure 9(c) shows the spin texture for strong spin-orbit coupling and weak magnetic field ($\Delta_{so}^D/E_0 = 1$, $\hbar\omega_c/E_0 = 0.1$) and finally, Fig. 9(d) shows the spin texture when both spin-orbit coupling and the magnetic field are strong ($\Delta_{so}^D/E_0 = 1$, $\hbar\omega_c/E_0 = 1$). The common features in all these cases are as follows.

(1) The $\hat{x}$ component of spin is zero at the wire center ($z = W_z/2$) as before but now it takes positive (negative) values for $z > W_z/2$ ($z < W_z/2$). This component can undergo another sign change depending on the strength of the spin-orbit coupling [see Figs. 9(c) and 9(d)], but again, it has opposite signs at the two edges as before. Comparing Figs. 7(a) and 9(a), we note that when both levels are occupied there is a sign reversal in $S_x(z)$.

(2) The magnitude of the $\hat{y}$ component is maximum and takes a positive value at the wire center ($z = W_z/2$) and becomes smaller toward the edges. For strong spin-orbit coupling [see Figs. 9(c) and 9(d)], the $\hat{y}$ component undergoes a sign change near the edges and become negative.

(3) Figure 9(b) shows the spin components of each spin-split band for weak spin-orbit coupling and weak magnetic field ($\Delta_{so}^D/E_0 = 0.06$, $\hbar\omega_c/E_0 = 0.1$). The spin components have opposite signs in the lower and upper bands, and hence the overall spin density is smaller due to this cancellation effect. The physical picture has been described before.

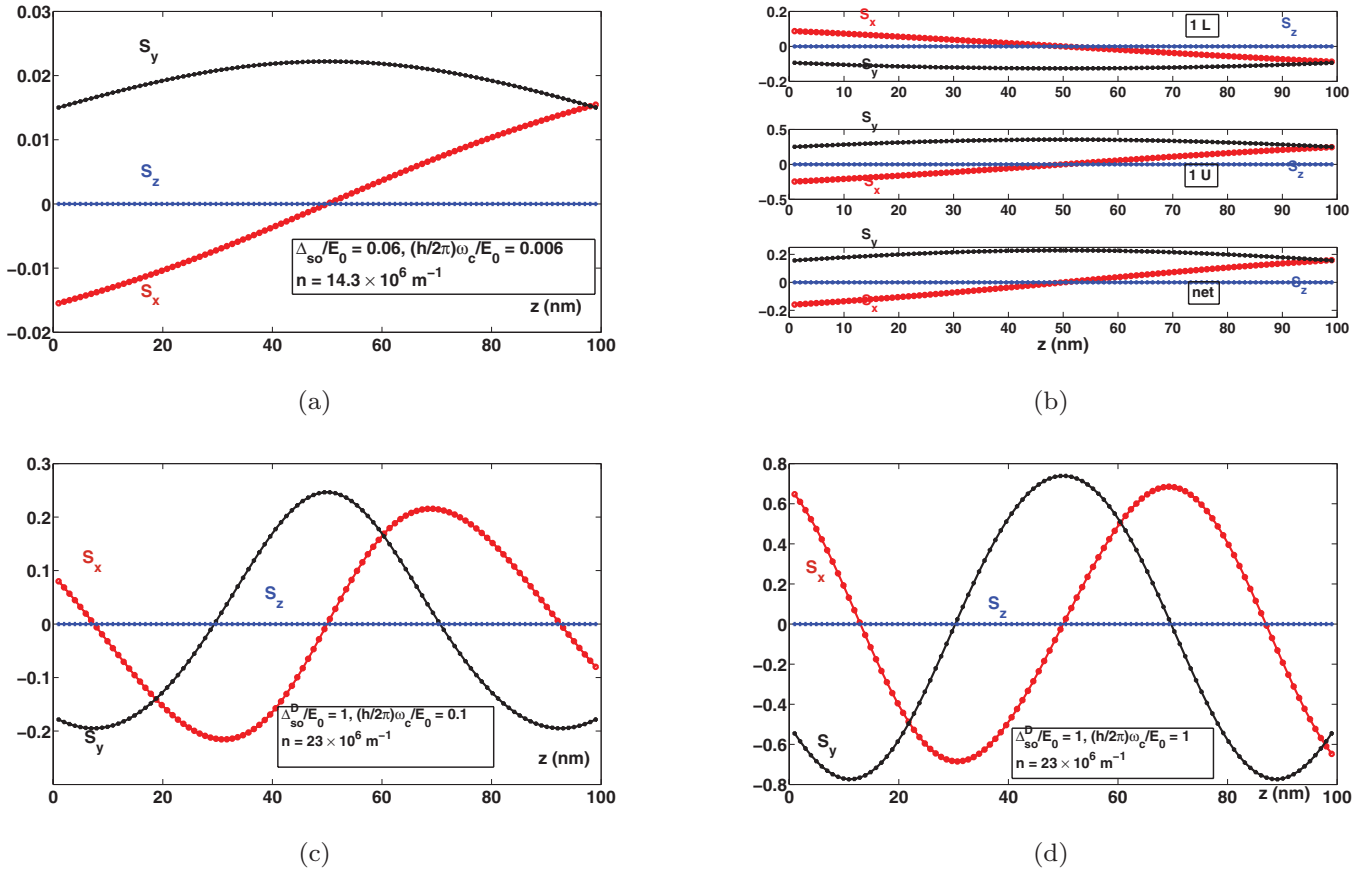

FIG. 9. (Color online) Spin texture for the case when both spin-split branches of the lowest subband are occupied. (a) Both spin-orbit coupling and magnetic field are weak ($\Delta_{so}^D/E_0 = 0.06$, $\hbar\omega_c/E_0 = 0.006$), (b) Spin texture for the lowest branch of subband 1 (1L, top panel), upper branch of subband 1 (1U, middle panel), and the net spin components (bottom panel) for weak spin-orbit coupling and weak magnetic field ($\Delta_{so}^D/E_0 = 0.06$, $\hbar\omega_c/E_0 = 0.1$), (c) Spin texture for strong spin-orbit coupling and weak magnetic field ($\Delta_{so}^D/E_0 = 1$, $\hbar\omega_c/E_0 = 0.1$) and (d) spin texture when both spin-orbit coupling and the magnetic field are strong ($\Delta_{so}^D/E_0 = 1$, $\hbar\omega_c/E_0 = 1$). In all cases, the lowest level ($1L$) has a camelback shape.

IV. SUMMARY AND CONCLUSION

To summarize, we have studied the effect of a transverse magnetic field on subband structure and spin texturing in a hard-wall quantum wire for a wide range of Dresselhaus spin-orbit coupling strength and various carrier concentrations. Even in the absence of any transport-driving electric field, Rashba effect, or terahertz radiation, a strong spin texturing can originate due to interaction between an external magnetic field and Dresselhaus spin-orbit coupling. These two ingredients are always present in typical spin accumulation experiments performed on zinc-blende quantum confined structures. We observe a $\pi/2$-phase shift between the transverse spin density components, which can be explained qualitatively in the weak spin-orbit regime. In presence of stronger spin-orbit interaction, stronger magnetic field, and larger carrier concentration, these features are preserved but the exact form of the modulation becomes more complex. Compared to the pure Rashba case, the spin texture does not quench in the high-magnetic-field limit, thus making this effect significant even when the Dresselhaus interaction is weak. These effects can be probed by the available experimental techniques and the magnetic field dependence of spin texture can be used to identify the dominant spin-orbit interaction in a zinc-blende quantum wire.

ACKNOWLEDGMENTS

This work is supported by the Disruptive Technology Challenge program (TRLabs, Canada) and NSERC, Canada.

*spramani@ualberta.ca

[1] I. Zutic, J. Fabian, and S. DasSarma, Rev. Mod. Phys. **76**, 323 (2004).
[2] J. Nitta, T. Akazaki, H. Takayanagi, and T. Enoki, Phys. Rev. Lett. **78**, 1335 (1997).
[3] S. Datta and B. Das, Appl. Phys. Lett. **56**, 665 (1990).
[4] S. Bandyopadhyay and M. Cahay, Appl. Phys. Lett. **85**, 1814 (2004).
[5] M. W. Wu, J. H. Jiang, and M. Q. Weng, Phys. Rep. **493**, 61 (2010).
[6] E. I. Rashba, Sov. Phys. Solid State **2**, 1109 (1960).
[7] G. Dresselhaus, Phys. Rev. **100**, 580 (1955).
[8] B. Das, S. Datta, and R. Reifenberger, Phys. Rev. B **41**, 8278 (1990).
[9] G. Engels, J. Lange, T. Schäpers, and H. Lüth, Phys. Rev. B **55**, R1958 (1997).
[10] S. Ganichev, E. Ivchenko, V. Belkov, S. Tarasenko, M. Sollinger, D. Weiss, W. Wegscheider, and W. Prettl, Nature (London) **417**, 153 (2002).
[11] A. Fedorov, Y. V. Pershin, and C. Piermarocchi, Phys. Rev. B **72**, 245327 (2005).
[12] A. V. Moroz, and C. H. W. Barnes, Phys. Rev. B **60**, 14272 (1999).
[13] A. V. Moroz and C. H. W. Barnes, Phys. Rev. B **61**, R2464 (2000).
[14] P. Upadhyaya, S. Pramanik, and S. Bandyopadhyay, Phys. Rev. B **77**, 155439 (2008).
[15] P. Upadhyaya, S. Pramanik, S. Bandyopadhyay, and M. Cahay, Phys. Rev. B **77**, 045306 (2008).
[16] S. Pramanik, S. Bandyopadhyay, and M. Cahay, Phys. Rev. B **76**, 155325 (2007).
[17] R. Winkler, Phys. Rev. B **69**, 045317 (2004).
[18] M. Governale and U. Zülicke, Phys. Rev. B **66**, 073311 (2002).
[19] Y. K. Kato, R. C. Myers, A. C. Gossard, and D. D. Awschalom, Science **306**, 1910 (2004).
[20] D. V. Khomitsky, Phys. Rev. B **79**, 205401 (2009).
[21] D. V. Khomitsky, Phys. Rev. B **77**, 113313 (2008).
[22] A. A. Perov, L. V. Solnyshkova, and D. V. Khomitsky, Phys. Rev. B **82**, 165328 (2010).
[23] J. Wunderlich, B. Kaestner, J. Sinova, and T. Jungwirth, Phys. Rev. Lett. **94**, 047204 (2005).
[24] M. Bode, M. Getzlaff, and R. Wiesendanger, Phys. Rev. Lett. **81**, 4256 (1998).
[25] D. Rugar, R. Budakian, H. J. Mamin, and B. W. Chui, Nature (London) **430**, 329 (2004).
[26] L. Meier, G. Salis, E. Gini, I. Shorubalko, and K. Ensslin, Phys. Rev. B **77**, 035305 (2008).
[27] M. Cardona, N. E. Christensen, M. Dobrowolska, J. K. Furdyna, and S. Rodriguez, Solid State Commun. **60**, 17 (1986).
[28] M. Cardona, N. E. Christensen, and G. Fasol, Phys. Rev. B **38**, 1806 (1988).
[29] M. Studer, M. P. Walser, S. Baer, H. Rusterholz, S. Schön, D. Schuh, W. Wegscheider, K. Ensslin, and G. Salis, Phys. Rev. B **82**, 235320 (2010).
[30] S. Zhang, R. Liang, E. Zhang, L. Zhang, and Y. Liu, Phys. Rev. B **73**, 155316 (2006).
[31] J. Knobbe and T. Schäpers, Phys. Rev. B **71**, 035311 (2005).
[32] S. Debald and B. Kramer, Phys. Rev. B **71**, 115322 (2005).
[33] W. Häusler, Phys. Rev. B **63**, 121310 (2001).
[34] T. Y. Zhang, W. Zhao, and X. M. Liu, J. Phys. Condens. Matter **21**, 335501 (2009).
[35] J. Cibert, P. M. Petroff, G. J. Dolan, S. J. Pearton, A. C. Gossard, and J. H. English, Appl. Phys. Lett. **49**, 1275 (1986).
[36] F. E. Prins, G. Lehr, M. Burkard, H. Schweizer, M. H. Pilkuhn, and G. W. Smith, Appl. Phys. Lett. **62**, 1365 (1993).
[37] A. Yacoby, H. L. Stormer, N. S. Wingreen, L. N. Pfeiffer, K. W. Baldwin, and K. W. West, Phys. Rev. Lett. **77**, 4612 (1996).
[38] T. Shitara, M. Tornow, A. Kurtenbach, D. Weiss, K. Eberl, and K. V. Klitzing, Appl. Phys. Lett. **66**, 2385 (1995).
[39] M. I. D'yakonov and V. Y. Kachorovskii, Fiz. Tekh. Poluprovodn. **20**, 178 (1986).
[40] S. Bandyopadhyay and M. Cahay, *Introduction to Spintronics* (CRC Press, 2008).
[41] M. Cahay and S. Bandyopadhyay, Phys. Rev. B **69**, 045303 (2004).